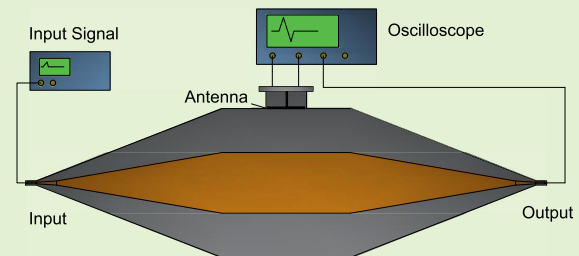


Design and Characterization of a Magnetic Loop Antenna for Partial Discharge Measurements in Gas Insulated Substations

Christian Mier Escurra¹, Armando Rodrigo Mor, and Peter Vaessen

Abstract—A recent investigation explored a new measuring concept used in partial discharges (PD) measurements in gas insulated substations (GIS), consisting of a magnetic loop antenna. The sensor's frequency response was characterized up to some tens of MHz. This paper proposes an improved version of the sensor with an extended bandwidth (BW) one order of magnitude higher: a resonance, attributed to a common mode current in the mounting hole, is identified and eliminated employing ferrite beads in the feeder cables. Moreover, this publication proposes an electric circuit model that fully covers the transverse electromagnetic mode (TEM) frequency range in GIS. The electric model is compared against experimental measurements using a 1 GHz bandwidth testbench, giving accurate results. Two contributions are achieved in this research: an improved magnetic loop antenna with extended bandwidth and an accurate electric circuit model. This publication paves the way for further research on time resolution and signal postprocessing techniques for magnetic loop antennas in GIS.

Index Terms—Magnetic loop antenna, partial discharges, transfer function, electric circuit, GIS, broadband antenna, VHF, high voltage.



I. INTRODUCTION

GAS insulated substations (GIS) exhibit advantages over traditional air insulated substations, such as long life span, high reliability, and reduced space. The reduced dimension of the GIS is crucial for remote locations like offshore wind farms where space is scarce and expensive. An electric failure in such outlying sites could compromise the entire substation; therefore, reliable remote monitoring of the GIS's insulation condition is needed. An accepted method for insulation diagnosis is partial discharges (PD) measurements, and in many cases, it is a requirement in the acceptance protocol [1].

Manuscript received May 25, 2021; accepted May 31, 2021. Date of publication June 14, 2021; date of current version August 31, 2021. This project (19ENG02 FutureEnergy) has received funding from the EMPIR programme co-financed by the Participating States and from the European Union's Horizon 2020 research and innovation programme. Funder ID: 10.13039/100014132. The associate editor coordinating the review of this article and approving it for publication was Dr. Santosh Kumar. (Corresponding author: Christian Mier Escurra.)

Christian Mier Escurra and Peter Vaessen are with the Department DC Systems, Energy Conversion and Storage, Delft University of Technology, 2628 CN Delft, The Netherlands (e-mail: c.mierescurra@tudelft.nl; p.t.m.vaessen@tudelft.nl).

Armando Rodrigo Mor is with the Instituto de Tecnología Eléctrica at Universitat Politècnica de València, 46022 Valencia, Spain, and also with the Delft University of Technology, 2628 CN Delft, The Netherlands (e-mail: arrodmor@ite.upv.es).

Digital Object Identifier 10.1109/JSEN.2021.3089084

A partial discharge is an acceleration of electric charges in a dielectric medium, which induces electromagnetic (EM) waves. The GIS guides the energy released by PD as a coaxial waveguide, where three modes can propagate depending on the frequency: transverse electromagnetic (TEM), transverse electric (TE), and transverse magnetic (TM). The last two propagation modes are complicated to evaluate.

The PD charge magnitude provides an estimation of the severity of the insulation degradation; additionally, it harmonizes readings from different sensors [2]. Studies presented in [3] and [4] conclude that it is not possible to estimate the PD charge using the ultra-high frequency (UHF) range because of the complex propagation in the TE or TM mode. Additionally, [5] demonstrates that the charge information is found in the PD spectra's low-frequency range. Therefore, a PD sensor that measures in the TEM frequency ranges is, in principle, able to calculate the charge of PD.

Reference [6] shows a novel PD measuring system for GIS, consisting of a magnetic loop antenna (MLA) that measures the TEM mode's magnetic field. In [7], the authors show measurements of the proposed MLA using a testbench with a limited frequency response up to a few tens of MHz; also, the presented electric circuit is constructed with lumped elements, limiting the frequency response characterization.

This research work is a continuation of [7]. First, the design of a calibration testbench with an extended frequency range



Fig. 1. Picture of the Testbench used to characterize PD antennas in GIS.

up to the UHF range is shown. This calibration setup is used for the experimental characterization of the magnetic loop antenna and has been instrumental in identifying the antenna's resonances. Secondly, an optimized antenna design to suppress the resonances is presented in this paper, along with a detailed mathematical model that accurately describes the antenna's response up to and including the UHF range. By extending the bandwidth (BW) of the sensor, a higher gain is achieved. Furthermore, the increased BW improves the charge estimation and the time resolution by decreasing reflected pulses overlapping [2].

II. CALIBRATION SETUP

A testbench covering the BW of the antennas was built, enabling measurements of the antenna's frequency and time response. The characteristic impedance through the testbench is matched to avoid reflections. Since the instruments used in PD measurements have an input impedance of 50Ω , the testbench is designed as a coaxial waveguide; the ratio between the outer and inner conductors (r_o and r_i) is 2.3:1, (1). For the antenna's frequency response characterization, a vector network analyzer (VNA) is used. The signal is transmitted from the VNA to the GIS by an N-type connector. The N-type connector has a small diameter relative to the GIS's diameter; hence, a transition-cone is used to maintain a gradual growth from the N-type connector's diameter to the GIS section. The transition-cones were handcrafted in a workshop: the inner conductor was made of paperboard covered with aluminum foil; the outer cones were hand-rolled using a 1 mm thick aluminum sheet, and aluminum flanges were welded at the base and vertex of the cones. Fig. 1 shows a photo of the resulted testbench.

$$Z_0 = \sqrt{\frac{\mu}{\epsilon}} \frac{\ln\left(\frac{r_o}{r_i}\right)}{2\pi}. \quad (1)$$

Fig. 2 shows the test setup used for the frequency response measurement; one cone's termination is connected to the VNA input, the other cone is terminated to a 50Ω load. The antenna's output is connected to the VNA port or through a signal conditioning device (filter and amplifier). A similar test setup is built for measurements in the time domain: the cone input and antenna's output are connected to an oscilloscope. A pulse source is connected to the other cone (see the abstract's figure). By using the dimensions presented in fig. 2, fig. 3 illustrates the frequency response of the testbench. As can be seen, the transmission parameter (S21)

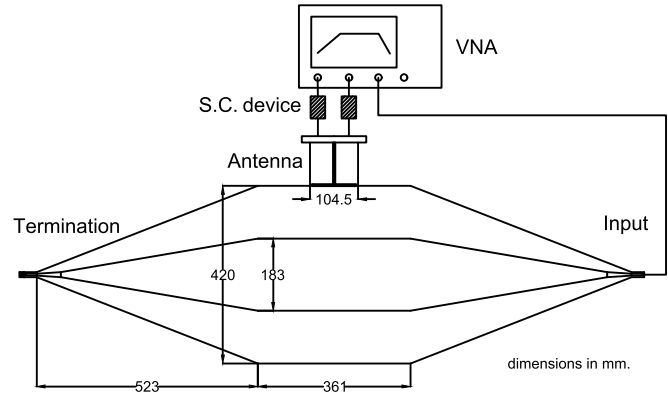


Fig. 2. Test-setup dimensions and configuration for measuring antennas' frequency response.

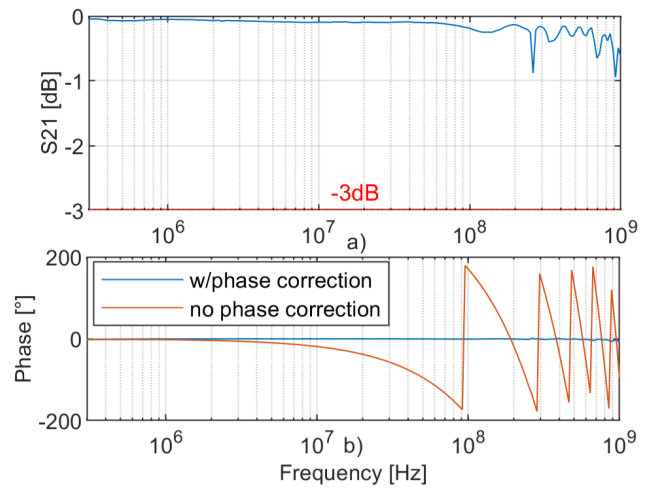


Fig. 3. Testbench frequency response a) magnitude and b) phase: with and without time delay correction.

TABLE I
TE MODE CUTOFF FREQUENCY FOR DIFFERENT GIS

GIS	Cutoff frequency
420 kV AC GIS	284 MHz
Testbench	300 MHz
320 kV DC GIS	332 MHz

results above -1dB up to 1 GHz. The time delay is corrected using (2), where: l is the length between the N-type connector input and the antenna, c is the speed of light in vacuum, f is the frequency, and ϕ is the phase delay.

$$\phi = 2\pi f \sqrt{\epsilon} \frac{l}{c}. \quad (2)$$

The sensor's high cutoff frequency must be below the TE mode to correctly estimate the PD charge. In (3), the coaxial cutoff frequency of the first high-order TE mode is presented. Table I shows the cutoff frequencies for the testbench and commercial 320 kV DC and a 420 kV AC GIS.

$$f_0 = \frac{c}{\pi \sqrt{\epsilon_r} (r_i + r_o)}. \quad (3)$$

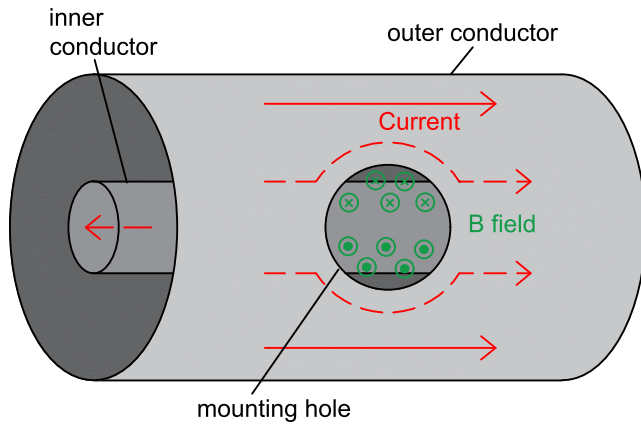


Fig. 4. PD's magnetic field induced in the GIS's mounting hole.

III. MAGNETIC LOOP ANTENNA'S BANDWIDTH

Partial discharges are electrically represented as current pulses; the PD charge magnitude is related to the current [5]. The gain of PD sensors is commonly expressed as the measured voltage (V_o) and the PD current (I_{pd}) ratio. In the following sections, the gain of the sensors is defined in $dB\Omega$, which is calculated as in (4).

$$G(\omega) = 20 \log \left(\left| \frac{V_o(\omega)}{I_{PD}(\omega)} \right| \right) [dB\Omega] \quad (4)$$

In a GIS, PD are current pulses that flow uniformly in the inner and outer conductor. Reference [6] demonstrates that the current induces a magnetic field at the mounting hole (fig. 4); this field is picked up with the magnetic loop antenna.

Two different MLAs are investigated in this paper: an unshielded and a shielded magnetic antenna. The unshielded magnetic loop antenna (UMLA) is described in fig. 5; it consists of a loop printed in a PCB, the terminals of the loop are connected to the inner and outer pin of an SMA connector. The shielded magnetic loop antenna (SMLA) consists of a shielded loop made of RG174A-U coaxial cable. At the loop's termination, the inner conductor is connected to the coaxial cable's shield, and the outer conductor is open-circuited (fig. 6). Additional information on the connection can be seen in the next section. In both antennas, the shield of the feeder coaxial cable is grounded to the mounting hole lid. A detailed explanation of the shielded antenna is given in [6].

The magnetic loop antenna is designed to capture the maximum amount of magnetic field produced by the PD. The antenna's loops cover the mounting hole area; a small gap of few millimeters is left between the loop and the GIS's neck. By Finite Element Method (FEM) and experimentation, it was found that most of the PD current flows through the upper edge of the neck (illustrated in red in fig. 6); hence, the MLA is matched to this plane. The dimensions are shared for both antennas and are indicated in fig. 5. In the case of the SMLA, the gap between the open circuit and the feeder cable is about 10 mm.

Fig. 7 a) and b) present a comparison of the magnitude and phase of the two antennas. As can be seen, the antennas show a slope in the low-frequency range due to the mutual inductance

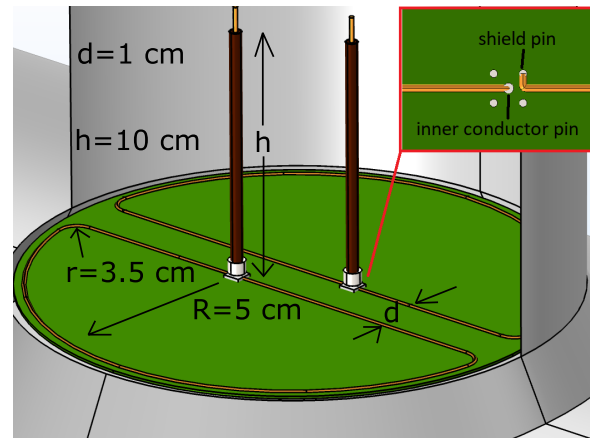


Fig. 5. PCB unshielded loop antenna sketch with a zoom of the loop connection to the SMA pins. General dimensions for the magnetic loop antennas.

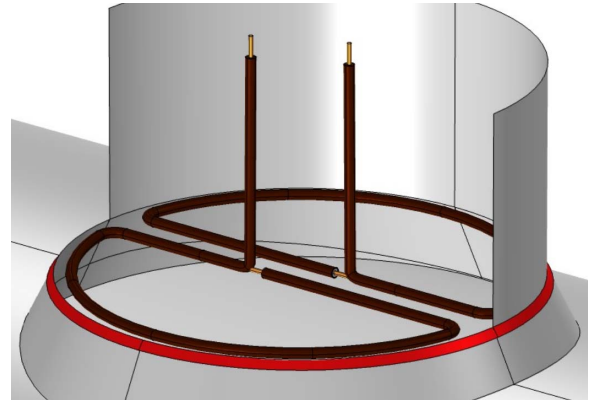


Fig. 6. Coaxial shielded loop antenna sketch. Represented in red is the concentration of current in the mounting hole neck.

between the GIS's mounting hole and the loop. After some tens of MHz, the sensor reaches a flat area influenced by the loop's self-inductance and the load impedance. Another notable result is the resonance at 150 MHz and 200 MHz for the shielded and unshielded antenna, respectively. Other resonances appear at higher frequencies; however, they are above the TEM propagation mode (see table I).

Reference [8] shows that PD in SF6 have ultra-high frequency spectra. An UHF pulse calibrator with a rise time of 640 ps was used to simulate PD pulses in the frequency range of the testbench. The antenna outputs were connected with 25 dB, 1 GHz bandwidth, voltage amplifiers. An intentional delay between signals was introduced to better visualize the results in the time domain. Authors in [9] show that it is possible to discriminate interference from PD signal by using symmetric lobes in each half of the mounting hole; the following plots in the time domain show the symmetry of the measurements when the signal is injected uniformly in the GIS.

Fig. 8 a) and b) show the measured pulses for the shielded and unshielded antennas, respectively. The unshielded sensor presents more oscillation than the case of the shielded sensor; this extra oscillation is attributed to an external electric field coupled to the antenna.

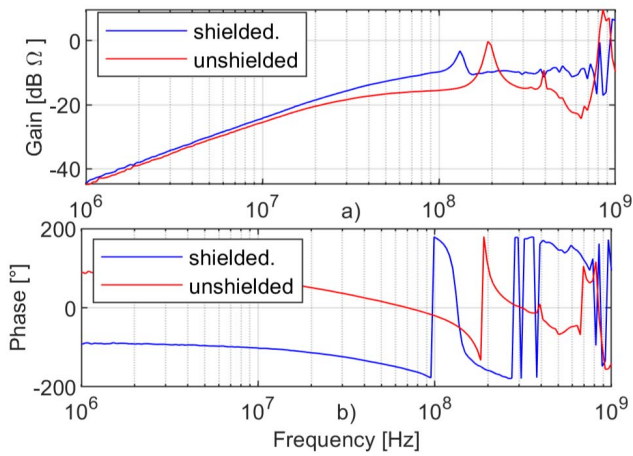


Fig. 7. Shielded and unshielded loop antenna frequency response, a) magnitude and b) phase.

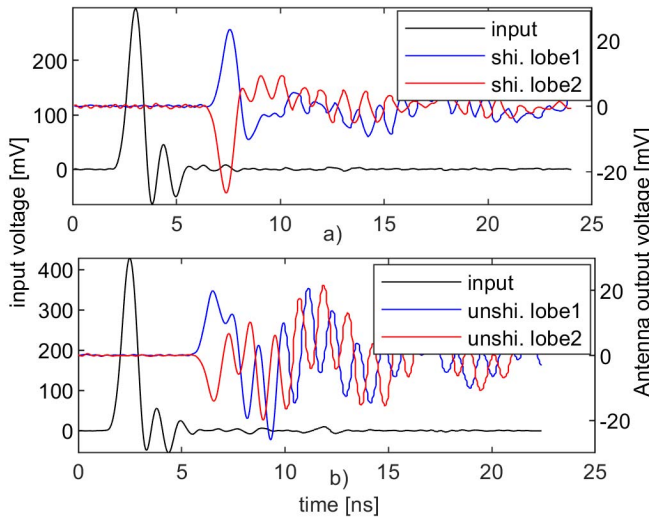


Fig. 8. UHF pulse measured with symmetric lobes in a) shielded and b) unshielded, magnetic antenna.

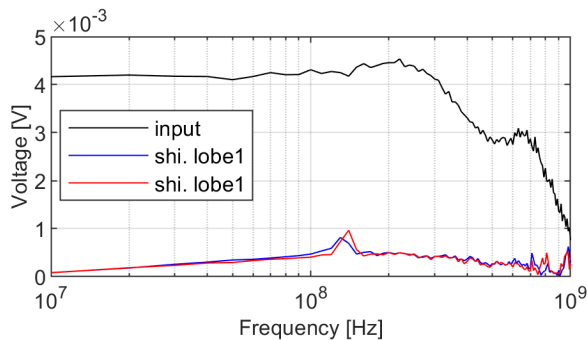


Fig. 9. FFT of the input pulse and shielded antenna's output.

Fig. 9 shows the Fast Fourier Transform (FFT) of the SMLA's measured pulse. The output measurements show a resonance at the same frequency as in fig. 7, demonstrating that the oscillation is a product of the antenna's resonance. The oscillation is generated by the gap capacitance

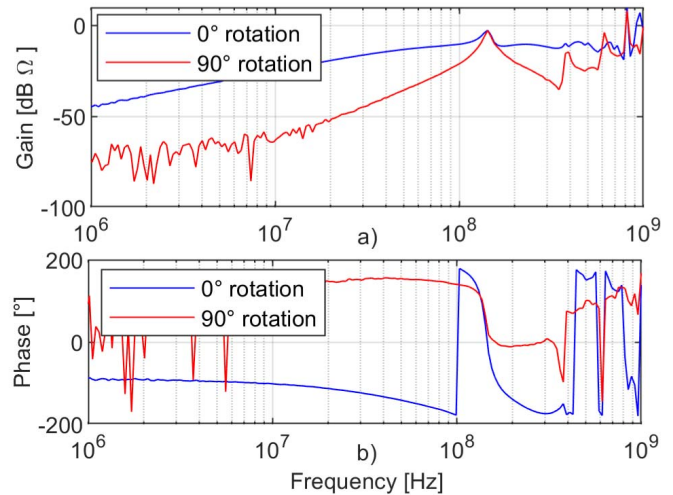


Fig. 10. Bode plot of the antenna positioned at 0° (in blue) and 180° (in red), a) magnitude and b) phase.

(between the antenna and the mounting hole) and the antenna's self-inductance. A common mode current (CMC) flows in the antenna at the resonance frequency; this current is identified in other loop antenna applications [10]. Following up are some reasons that support the previous hypothesis:

- When the aluminum lid of the mounting hole is replaced by plastic, the resonance disappears: there is no conductive path for the CMC to circulate.
- If the antenna is rotated 90°, no voltage is induced in the loop [6]. However, the resonance is maintained at almost the same frequency: the capacitance and the self-inductance are kept. In fig. 10 a) and b), we can see that the amplitude and phase of the antenna are the same, irrespectively of the rotation.
- If the antenna is further introduced in the direction of the mounting hole axis, the resonance frequency is shifted: the capacitance in the gap changes.

It was discovered that the CMC is eliminated by employing a ferrite bead clamped in the feeder coaxial cable (see fig. 11). At the resonance frequency, the CMC flows in only one direction of the feeder cable, inducing a magnetic field in the ferrite; the fluctuating field causes losses in the ferrite, which causes resistance in the feeder cable, eliminating the resonance (fig. 12).

Fig. 13 shows the frequency response for the UMLA and SMLA with the implementation of the ferrite. A Fair-Rite ferrite (part number: 443164251) was used; the ferrite induces almost 300 Ohms at the resonance frequency. A broad flatness is observed in the Bode plot in fig. 13. The shielded magnetic antenna shows superior gain over the unshielded sensor; this is attributed to the higher self-inductance of the unshielded antenna. A detailed explanation is found in the next section. Additionally, the SMLA has better electric field interference rejection; further analysis does not include the unshielded sensor.

Fig. 14 a) shows the antennas' response to the UHF calibration pulse using the ferrite; in b), an additional 250 MHz

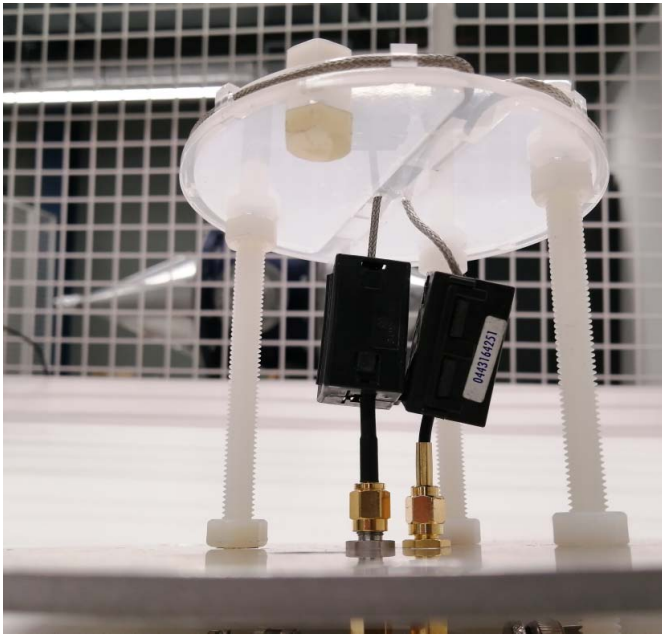


Fig. 11. Picture of the ferrites clamped in the antenna's feeder cables.

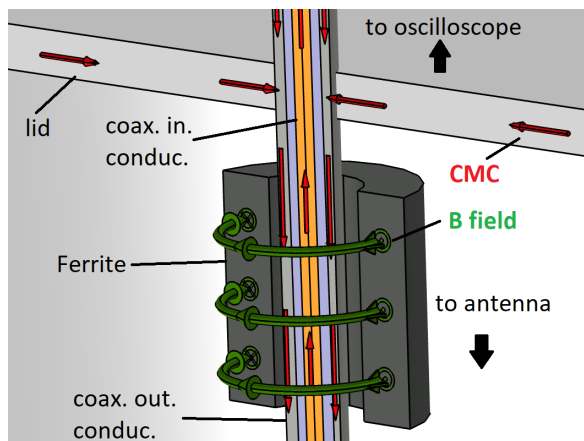


Fig. 12. Magnetic field induced in the ferrite due to the common mode current.

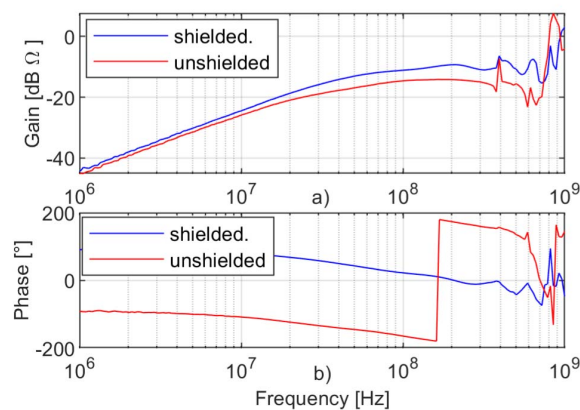


Fig. 13. Frequency response of shielded and unshielded loop antenna using a ferrite, a) magnitude, and b) phase.

1st order filter is included. By filtering the signal, higher frequency resonances are eliminated; in a real GIS, these resonances may contain the three modes of propagation (table I).

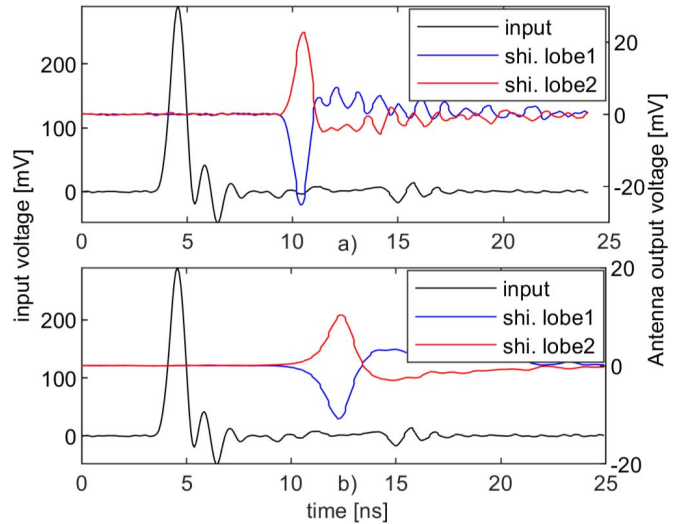


Fig. 14. Time domain response of a shielded loop antenna to the UHF pulse, using a ferrite a) without filter and b) with a 250 MHz filter.

The filtered pulses have an increased duration, making them prone to overlap with reflected pulses in a real GIS. Therefore, the BW of the filter must be properly analyzed to produce a signal with enough sensitivity and time resolution.

IV. ELECTRIC CIRCUIT

A mathematical model of the antenna helps to understand the impact of each electric element on the design. Reference [7] proposes the antenna's electric circuit as lumped elements; the antenna's length is about 30 cm, compared with the wavelength the electric circuit is valid below 100 MHz. To extend the frequency range of this model, the coaxial loop is treated as a transmission line.

According to [11] and [12], when the current depth of penetration is less than 10% of the shield thickness, the external magnetic field only induces EMF in the outer layer of the shield: the inner layer of the shield and the inner conductor of the coaxial line do not interact with the external fields. The loop of the outer-shield layer induces a voltage at the gap terminals (V_c); this voltage is seen by the inner layer shield and the inner conductor (fig. 15).

Following the previous explanation, fig. 16 illustrates the electric circuit of the antenna. The outer shield current mesh, colored in red, is represented by (5), where V_{in} is the voltage source, L_s is the self-inductance of the outer shield, and C is gap capacitance (6). The GIS PD current (I_{pd}) induces a voltage V_{in} in the outer shield; this coupling depends on the mutual inductance (M) between the antenna and the GIS (7).

$$V_{in} = j\omega L_s I_s + V_c \quad (5)$$

$$V_c = -\frac{jI_c}{\omega C} \quad (6)$$

$$V_{in} = j\omega I_{pd} M \quad (7)$$

At the gap, the shield current is divided between the gap capacitance and the inner layer of the shield (8).

$$I_s = I_1 + I_c \quad (8)$$

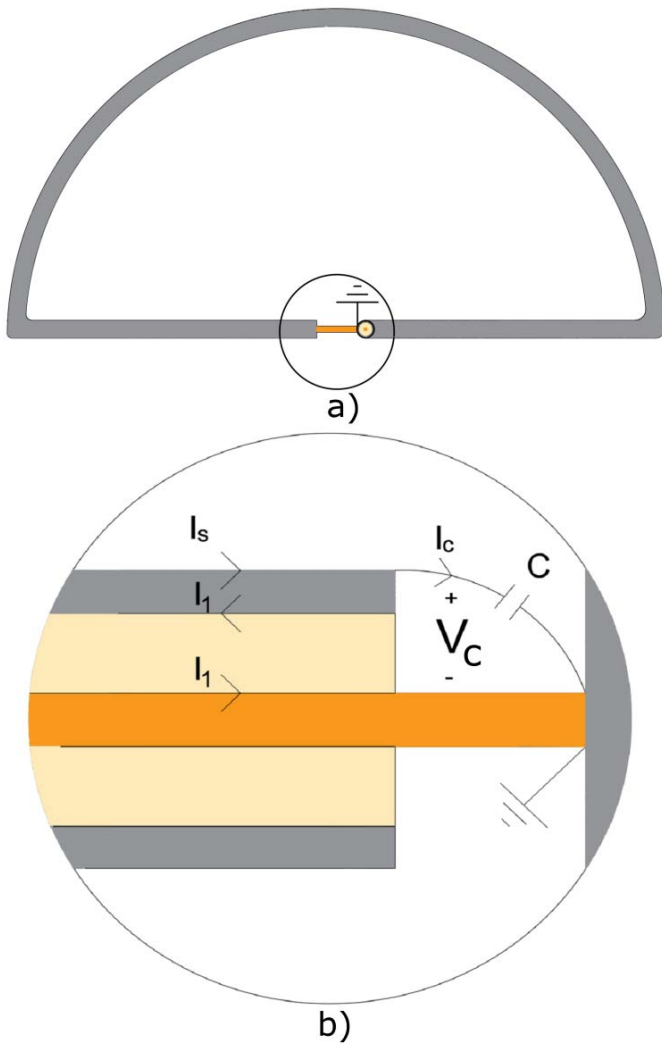


Fig. 15. a) shielded loop top view. b) amplification of the inner conductor connected to the feeder shield.

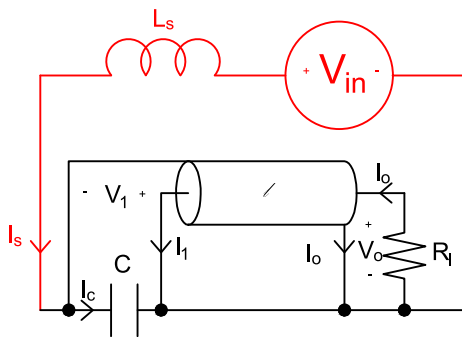


Fig. 16. Electric circuit diagram of the shielded loop antenna.

In parallel with the gap capacitance (9) is the input impedance (10) seen at the coaxial cable input (11).

$$V_c = -V_1 \quad (9)$$

$$Z_{in} = Z_0 \frac{R_l + jZ_0 \tan(\beta l)}{Z_0 + jR_l \tan(\beta l)} \quad (10)$$

$$V_1 = -I_1 Z_{in} \quad (11)$$

The voltage in any point of the coaxial cable is calculated with (12). Where z is the distance propagated in the coaxial cable and β is the propagation constant for a lossless line: $\beta = \omega Z_0 C_c$, C_c is the capacitance per unit length, and Z_0 the characteristic impedance of the coaxial cable. Additionally, Γ_l is the voltage reflection coefficient at the load's terminals and is calculated in (13):

$$V(z) = V_0^+ (e^{-j\beta z} + \Gamma_l e^{j\beta z}) \quad (12)$$

$$\Gamma_l = \frac{Z_l - Z_0}{Z_l + Z_0} \quad (13)$$

When (12) is analyzed at the total length of the line ($z = l$), and at the start of the coaxial cable ($z = 0$), it results in (14) and (15), respectively.

$$V(-l) = V_1 = V_0^+ (e^{j\beta l} + \Gamma_l e^{-j\beta l}) \quad (14)$$

$$V(0) = V_o = \frac{V_1 (1 + \Gamma_l)}{(e^{j\beta l} + \Gamma_l e^{-j\beta l})} \quad (15)$$

where V_o is the voltage at the load R_l .

By substituting equations (9) into (6) and (8) and (11) into (5), we get:

$$V_{in} = -j\omega L_s \frac{V_1}{Z_{in}} + \omega^2 L_s C V_1 - V_1 \quad (16)$$

Finally, by replacing (7) and (15) into (16) and rearranging, the transfer function (TF) results in:

$$\frac{V_o}{I_{pd}} = \frac{-j\omega M (1 + \Gamma_l)}{(1 + j\omega L_s / Z_{in} - \omega^2 L_s C) (e^{j\beta l} + \Gamma_l e^{-j\beta l})} \quad (17)$$

If $R_l = Z_0$ and neglecting the 2nd order term for the TEM frequency range, the previous equation is reduced to:

$$\frac{V_o}{I_{pd}} = \frac{-j\omega M e^{-j\beta l}}{1 + j\omega L_s / R_l} \quad (18)$$

Equation (18) gives a similar result to the TF of the unshielded antenna (19), with two exceptions: a time delay caused by the coaxial loop, and a change of polarity of the output signal: this is observed in fig. 7 b) and fig. 13 b).

$$\frac{V_o}{I_{pd}} = \frac{j\omega M}{1 + j\omega L_s / R_l} \quad (19)$$

As mentioned before, the magnetic loop antenna consists of two symmetrical lobes (see figs. 5 and 6). One of the lobes induces a back EMF in the other lobe and vice versa; because the current in each lobe is equal, the induced back EMF can be represented by an increase in the self-inductance, rising an apparent self-inductance, $L_s = L_{self} + M_{lobes}$, where L_{self} is the self-inductance of the loop, and M_{lobes} is the mutual inductance between the lobes. Consequently, the magnetic coupling between the lobes of the antenna can be accounted for (18) and (19) using the apparent self inductance L_s .

All the values from the model can be calculated by experimentation, table II shows the values of the calculated parameters:

- Mutual inductance (M): reference [13] shows that the mutual inductance value approximates the TF's slope at low frequencies. A sinusoidal wave was injected into the

TABLE II
ELECTRIC CIRCUIT PARAMETERS OF THE LOOP ANTENNA

Parameter	Shielded Antenna	Unshielded Antenna
Mutual inductance (M)	0.96 nH	0.96 nH
Apparent self-inductance (L_s)	170 nH	290 nH
Mutual inductance between lobes (M_{lobes})	35.0 nH	30.0 nH
Self-inductance (L_{self})	135 nH	260 nH
Gap capacitance (C)	0.1-1.0 pF	Not Applicable

GIS and measured at the antenna's output; the mutual inductance is calculated using (20).

$$H(\omega) = \frac{V_o(\omega)}{I_{pd}(\omega)} \approx j\omega M \quad \text{when } \omega \rightarrow 0 \text{ rad/s} \quad (20)$$

- Apparent self-inductance (L_s): it is calculated by loading the antenna with a known capacitor (C_l) and measuring the resonance frequency. The calculation depends on the capacitor's location. When it is connected at the shield gap, the apparent self-inductance is calculated by (21), where ω_0 is the resonance frequency. However, if it is parallel with the load (R_l), (18) must be used, replacing R_l with the equivalent impedance of R_l in parallel with C_l . When a sufficiently big capacitor is used, the resonance occurs in a frequency where the wavelength is 10 times bigger than the transmission line length: the coaxial cable can be considered a lumped inductance and a lumped capacitance; the apparent self-inductance is simplified to (22).

$$L_s = \frac{1}{C_l \omega_0^2} \quad (21)$$

$$L_s = \frac{1}{(C_l + C_c) \omega_0^2} - Z_0^2 C_c \quad (22)$$

- Mutual inductance between lobes (M_{lobes}): it is calculated using (20), by injecting a sinusoidal voltage at one lobe and measuring at the other.
- Gap capacitance (C): The gap's capacitance is complicated to measure; however, by doing a FEM and by analytical calculation according to [11], an approximate value is obtained.

As shown in (18) and (19), an increase in self-inductance (L_s) reduces the sensor's gain. According to [10], circular loop inductances are calculated using (23), where b is the radius of the loop, and a is the radius of the conductor. A similar calculation is assumed for the antenna loop. The PCB's conductor diameter is considerably smaller than the coaxial shield diameter, explaining the shielded antenna's higher gain.

$$L_{self} = \mu_0 b \ln \frac{b}{a} \quad (23)$$

V. RESULTS

Fig. 17 compares the SMLA's measurements and the proposed model; the transfer functions approximate the experiment's magnitude and phase. The measured phase delay, caused by the coaxial loop of the SMLA, is not corrected

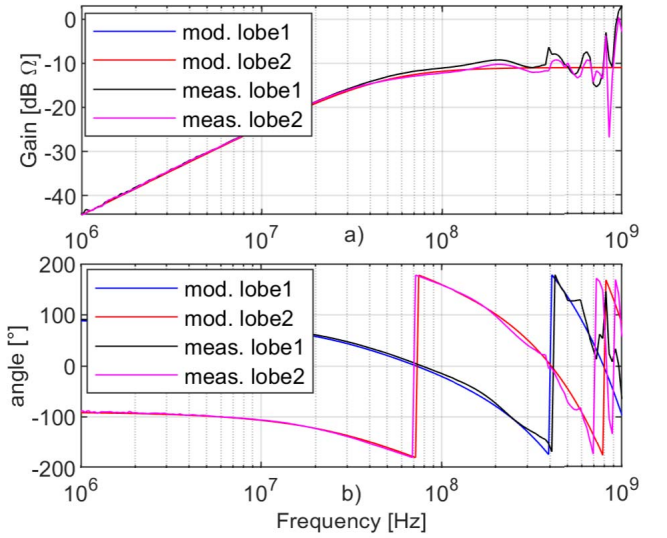


Fig. 17. a) magnitude and b) phase comparison between measurements and model of the SMLA.

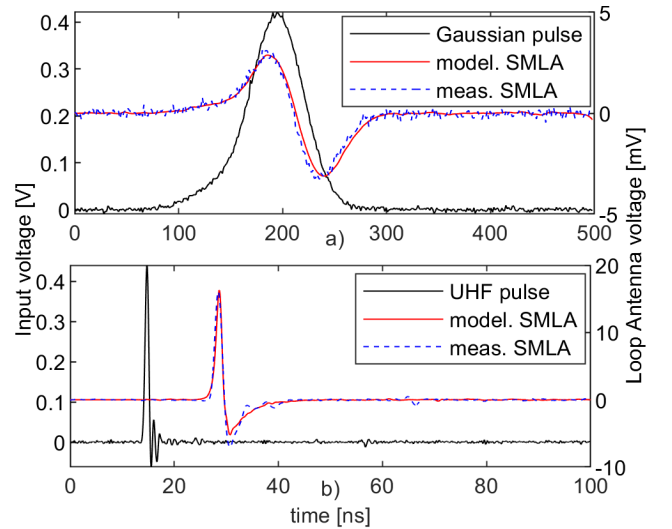


Fig. 18. Comparison between measurement and model for a) $\sigma = 25$ ns Gaussian input pulse and b) the UHF input pulse.

so that it can be compared with the phase delay expressed in (18).

By knowing the transfer function, it is possible to calculate the output voltage from the input pulse. Fig. 18 a) compares the measured and computed output signal for a $\sigma = 25$ ns Gaussian input pulse. In fig. 18 b), the UHF calibrator is used, and the output signal is processed with a 270 MHz, 1^{st} order filter. The simulated output pulses show a high resemblance to the measurements, validating the mathematical model.

VI. CONCLUSION

A testbench was built to measure the total bandwidth of magnetic loop antennas installed in GIS. A resonance at 150 MHz, attributed to a common mode current in the mounting hole, was eliminated employing ferrite beads in the

feeder cables. The bandwidth of the sensor was extended, from the previous investigation, about an order of magnitude.

In this paper, an electric model of the magnetic antenna is proposed; the model covers the frequency range of the TEM mode for any commercial GIS. The model is compared with measurements giving high accuracy. The measurements showed a better performance for the shielded loop antenna over the unshielded one. The antenna model helps to understand the impact of each electric element on the design; additionally, it helps to investigate the relation of the antenna with the charge estimation method.

REFERENCES

- [1] T. Gulski, M. Strehl, S. Muhr, and S. Tebohlen, "Guidelines for unconventional partial discharge measurements," CIGRE, Paris, France, Tech. Brochure, 2010, doi: [10.1109/JSEN.2017.2651028](https://doi.org/10.1109/JSEN.2017.2651028).
- [2] A. Cavallini, G. C. Montanari, and M. Tozzi, "PD apparent charge estimation and calibration: A critical review," *IEEE Trans. Dielectr. Electr. Insul.*, vol. 17, no. 1, pp. 198–205, Feb. 2010, doi: [10.1109/TDEI.2010.5412018](https://doi.org/10.1109/TDEI.2010.5412018).
- [3] G. Behrmann, S. Franz, J. Smajic, Z. Tanasic, and R. Christen, "UHF PD signal transmission in GIS: Effects of 90° bends and an L-shaped CIGRE step 1 test section," *IEEE Trans. Dielectr. Electr. Insul.*, vol. 26, no. 4, pp. 1293–1300, Aug. 2019, doi: [10.1109/TDEI.2019.008005](https://doi.org/10.1109/TDEI.2019.008005).
- [4] S. Ohtsuka, T. Teshima, S. Matsumoto, and M. Hikita, "Relationship between PD-induced electromagnetic wave measured with UHF method and charge quantity obtained by PD current waveform in model GIS," in *Proc. IEEE Conf. Electr. Insul. Dielectric Phenomena*, Oct. 2006, pp. 615–618.
- [5] A. R. Mor, P. H. F. Morshuis, and J. J. Smit, "Comparison of charge estimation methods in partial discharge cable measurements," *IEEE Trans. Dielectr. Electr. Insul.*, vol. 22, no. 2, pp. 657–664, Apr. 2015, doi: [10.1109/TDEI.2015.7076760](https://doi.org/10.1109/TDEI.2015.7076760).
- [6] A. Rodrigo-Mor, F. Muñoz, and L. Castro-Heredia, "A novel antenna for partial discharge measurements in GIS based on magnetic field detection," *Sensors*, vol. 19, no. 4, p. 858, Feb. 2019, doi: [10.3390/s19040858](https://doi.org/10.3390/s19040858).
- [7] A. Rodrigo Mor, L. C. Castro Heredia, and F. A. Muñoz, "A magnetic loop antenna for partial discharge measurements on GIS," *Int. J. Electr. Power Energy Syst.*, vol. 115, Feb. 2020, Art. no. 105514, doi: [10.1016/j.ijepes.2019.105514](https://doi.org/10.1016/j.ijepes.2019.105514).
- [8] A. J. Reid, M. D. Judd, B. G. Stewart, and R. A. Fouracre, "Partial discharge current pulses in SF₆ and the effect of superposition of their radiometric measurement," *J. Phys. D, Appl. Phys.*, vol. 39, no. 19, pp. 4167–4177, Oct. 2006.
- [9] F. Muñoz-Muñoz and A. Rodrigo-Mor, "Partial discharges and noise discrimination using magnetic antennas, the cross wavelet transform and support vector machines," *Sensors (Switzerland)*, vol. 20, no. 11, pp. 1–14, 2020, doi: [10.3390/s20113180](https://doi.org/10.3390/s20113180).
- [10] C. F. M. Carobbi and L. M. Millanta, "Analysis of the common-mode rejection in the measurement and generation of magnetic fields using loop probes," *IEEE Trans. Instrum. Meas.*, vol. 53, no. 2, pp. 514–523, Apr. 2004, doi: [10.1109/TIM.2004.823297](https://doi.org/10.1109/TIM.2004.823297).
- [11] L. L. Libby, "Special aspects of balanced shielded loops," *Proc. IRE*, vol. 34, no. 9, pp. 641–646, Sep. 1946.
- [12] L. V. Vasenkov and V. A. Tishchenko, "Design of a shielded loop antenna," *Meas. Techn.*, vol. 31, no. 8, pp. 796–798, Aug. 1988, doi: [10.1007/BF00863499](https://doi.org/10.1007/BF00863499).
- [13] A. Rodrigo-Mor, F. A. Muñoz, and L. C. Castro-Heredia, "Principles of charge estimation methods using high-frequency current transformer sensors in partial discharge measurements," *Sensors*, vol. 20, no. 9, p. 2520, Apr. 2020, doi: [10.3390/s20092520](https://doi.org/10.3390/s20092520).



Christian Mier Escurra was born in Aguascalientes, Mexico, in 1991. He received the bachelor's degree in mechanical and electrical engineering from ITESM, Monterrey, in 2014, and the master's degree in electrical engineering from the Delft University of Technology, Delft, The Netherlands, in 2018, where he is currently pursuing the Ph.D. degree. From 2014 to 2016, he worked as a Junior Engineer with Electric Power Consultancy Firm (Diram), Mexico. From 2018 to 2020, he worked as a Senior Engineer with Diram. His research interests include monitoring and diagnostic, high voltage engineering, transients, and power systems.



Armando Rodrigo Mor received the Ph.D. degree in electrical engineering from the Universitat Politècnica de València, Valencia, Spain. In Spain, he joined and later led the High Voltage Laboratory and the Plasma Arc Laboratory, Instituto de Tecnología Eléctrica, Valencia. From 2013 to 2021, he was an Assistant Professor with the Electrical Sustainable Energy Department and became the Head of the High Voltage Team, Delft University of Technology, Delft, The Netherlands, in 2019. Since 2021, he has been with the Instituto de Tecnología Eléctrica, Universitat Politècnica de València, where he is also an Industrial Engineer. His research interests include high-voltage technology, high-voltage testing, monitoring and diagnostic, sensors for high-voltage applications, space charge measurements, and HVDC.



Peter Vaessen received the M.Sc. (*cum laude*) degree in electrical power engineering from Eindhoven Technical University, The Netherlands, in 1985. He joined KEMA (currently CESI brand) in 1985. In his 35 years career, he held various research positions in the field of large power transformers and high voltage measurement and testing. He headed the Transmission and Distribution High Voltage Department and managed realization projects, including constructing Dutch 400 kV substations and laboratory test facilities.

As a Principal Consultant, he has 25 years of experience with (U)HVDC Technology and Transmission and Distribution Grids with high shares of renewables. He is the Manager of Innovations at CESI and actively involved in the technology strategy. He is the Chairman of the Board of the European Distributed Energy Resources Laboratories Association (DERlab) and a member of several national and international working groups. He is a part-time Professor of Hybrid Transmission Systems with TU Delft, where he teaches high voltage technology and HVDC.